*Key Engineering Materials*
*ISSN: 1662-9795, Vol. 1050, pp 1-7*
*doi:10.4028/p-4tzjOZ*

*Submitted: 2025-11-24*
*Revised: 2026-02-17*
*Accepted: 2026-02-17*
*Online: 2026-04-16*

# Numerical Investigation of Deposition Efficiency Influencing Factors in the Friction Surfacing Process

Ahmed Elbossily[1,a*], Zina Kallien[1,2,b], Rupesh Chafle[2,c], Kirk A. Fraser[3,d], Mohamadreza Afrasiabi[4,e], and Benjamin Klusemann[1,2,f]

[1]Institute for Production Technology and Systems, Leuphana Universität Lüneburg, Universitätsallee 1, 21335, Lüneburg, Germany

[2]Institute of Material and Process Design, Helmholtz-Zentrum Hereon, Max-Planck-Straße 1, 21502 Geesthacht, Germany

[3]National Research Council Canada, Saguenay, QC, Canada

[4]Advanced Manufacturing Lab, ETH Zurich, Zurich, Switzerland

[a]Ahmed.Elbossily@Leuphana.com, [b]zina.kallien@hereon.de, [c]rupesh.chafle@hereon.de, [d]kirk.fraser@cnrc-nrc.gc.ca, [e]afrasiabi@ethz.ch, [f]benjamin.klusemann@leuphana.de

**Keywords:** Numerical Study, Smoothed Particle Hydrodynamics, Friction Surfacing, Deposition Efficiency

**Abstract.** This work presents a numerical study of the friction surfacing process using a GPU - accelerated Smoothed Particle Hydrodynamics (SPH) framework previously validated against experimental observations. The model is employed to examine how thermal boundary conditions, rod diameter, and rod bending angle influence material deposition efficiency and the resulting deposit geometry. Variations in rod diameter are shown to influence both the thermal response and the contact pressure, with smaller rods producing higher efficiency but exhibiting greater process fluctuations. The findings highlight the critical roles of thermal management and geometric configuration in optimizing friction surfacing performance and provide actionable insight for experimental design and process control in solid-state deposition technologies.

## Introduction

Friction surfacing (FS) is a solid-state process that uses frictional heat and plastic deformation to deposit a consumable material. It minimizes distortion and further thermal effects while promoting dynamic recrystallization and producing a fine-grained microstructure [1]. These qualities make it useful for coating, repair, and additive manufacturing applications [2, 3, 4]. Although numerous experimental investigations have examined the FS process, numerical investigations remain relatively limited.

Early numerical investigations primarily employed the finite element method (FEM) to study the temperature field [5], where the deposition was modeled using element activation, neglecting actual material flow and thus limiting deposition formation prediction. Subsequent thermo-mechanical FEM analyses were developed [6, 7], but mesh-based approaches remain inadequate for capturing the severe deformations and material separation inherent to the FS process. Consequently, meshless methods such as Smoothed Particle Hydrodynamics (SPH) have emerged as a promising alternative [8].

Aval [9] developed a SPH model to simulate the FS process, demonstrating strong agreement with experimental data, and utilized it to analyze the effects of axial feeding rate and traverse speed on deposition efficiency and interface bonding [10, 11]. Elbossily et al. [12] introduced a GPU-based SPH framework for the FS process with computational optimizations and stability enhancements. A new material separation criterion based on shear stress was proposed to improve the simulation of the deposition behavior. Validated experimentally, the model captures key FS mechanisms such as material flow, rod flash formation, and deposition geometries for different process parameters, providing a robust tool for analyzing and optimizing FS processes.

This study utilizes the previously developed SPH model [12] to analyze deposition efficiency under varying substrate thermal boundary conditions, rod diameters, and rod bending angles.

**Model Setup**

Fig. 1a shows the SPH model setup used in this study, including the geometries, materials, and the number of SPH particles. The initial spacing between all SPH particles is set to 1 mm, which is selected to balance model prediction accuracy with simulation run time. The SPH model consists of two deformable bodies: a rotating rod and a substrate. During the deposition process, the substrate translates laterally at a constant traverse speed, while material is deposited onto its surface, Fig. 1b. Thermal dissipation occurs via convection through the model's external surfaces. The material behavior is modeled using the Johnson-Cook constitutive model [13]. Details regarding the material properties and simulation parameters are available in [12].

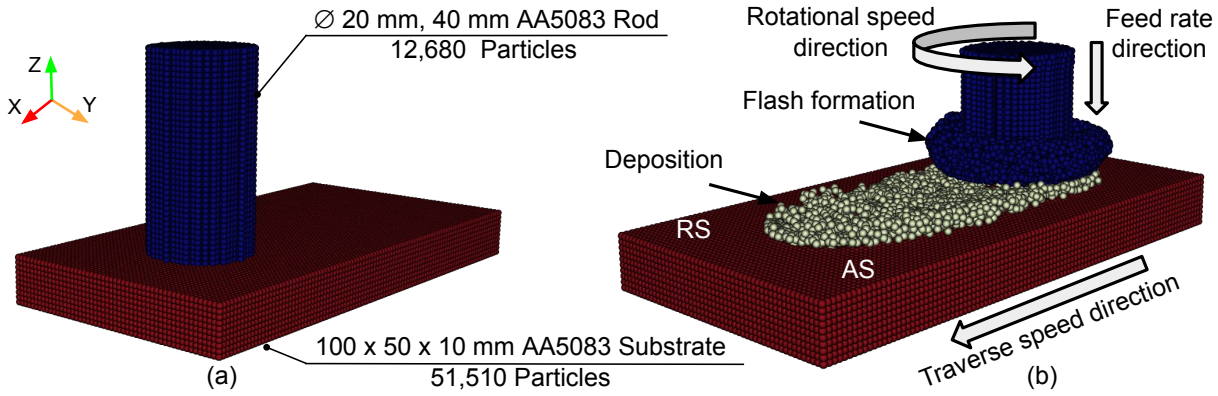


Fig. 1: FS model: (a) main dimensions, material type, and particle count; (b) visualization of rod feed direction, rod rotation direction, substrate traverse speed direction, advancing side (AS), retreating side (RS), and the resulting rod flash and material deposition at the end of the simulation.

**Joining criterion.** The joining criterion proposed by Elbossily et al. [12] is revised to be independent of the joining temperature. This modification reduces the numerical constraints on the deposition behavior, while the temperature influence remains captured through the material's temperature-dependent shear strength $\tau_i^{allow}$. By eliminating the joining temperature as an input parameter, deposition is no longer forced to occur at a predefined temperature threshold, which previously mimicked a binary (0 or 1) condition and could not reflect realistic material behavior. The joining criterion is defined as

$$\text{Joined}_i = \begin{cases} 1, & (\tau_i \geq \tau_i^{allow}) \wedge (\varepsilon_i^{pl} \geq 0.01) \\ 0, & \text{Otherwise} \end{cases} \tag{1}$$

where $\varepsilon_i^{pl}$ and $\tau_i$ are the plastic strain and the shear stress of the particle $i$, respectively.

**Simulation sets.** The numerical study includes seven simulation sets to evaluate the influence of the substrate thermal boundary conditions and the rod geometric variations on the FS process. Set 0 is the reference simulation, with heat loss to the surroundings modeled via a free convection coefficient of 5 $W/m^2\,^\circ C$ from the substrate's sides and bottom surfaces. A higher heat convection coefficient of 1000 $W/m^2\,^\circ C$ is employed on the rod top surface to mimic heat dissipation to the rest of the rod following the approach by Zou et al. [17]. Set 1 introduces substrate preheating by initializing the temperature of the substrate at 200 $^\circ C$ and applying a constant temperature of 200 $^\circ C$ to the bottom surface of the substrate. Set 2 imposes cooling conditions by increasing the heat convection to 5000 $W/m^2\,^\circ C$ for the substrate's sides and bottom surfaces. The next two sets modify the rod geometry by increasing the rod diameter from 20 mm to 25 mm in Set 3 and reducing it to 15 mm in Set 4. The last two setups examine potential rod bending during the process. In Sets 5 and 6, bending

Table 1: Summary of the simulation sets and corresponding process setup, including substrate boundary conditions (applied heat convection value $h_c$ and initial temperature $T_{init}$), rod diameter, and rod bending angle.

| set | simulation setup | substrate $h_c$ $(W/m^2\,°C)$ | substrate $T_{init}$ $(°C)$ | rod diameter (mm) | bending angle $(°)$ |
|---|---|---|---|---|---|
| 0 | reference | 5 | 20 | 20 | 0 |
| 1 | heated | 5 | **200** | 20 | 0 |
| 2 | cooled | **5000** | 20 | 20 | 0 |
| 3 | bigger diameter | 5 | 20 | **15** | 0 |
| 4 | smaller diameter | 5 | 20 | **25** | 0 |
| 5 | bending 5° | 5 | 20 | 20 | **5** |
| 6 | bending 10° | 5 | 20 | 20 | **10** |

angles of 5° and 10°, respectively, are applied relative to the vertical axis at the rod clamping position. The chosen bending angles are relatively large to ensure noticing the rod bending effect, given the rod's short length used in the simulation. The process parameters remain constant across all simulations: 900 rpm rotational speed, 1.8 mm/s rod feed rate, and 6 mm/s substrate traverse speed. Table 1 summarizes the investigated simulation conditions.

**Results and Discussion**

This section discusses the deposition efficiency for all sets summarized in Table 1. Deposition efficiency quantifies how effectively the rod material is utilized during the process. It is defined as the ratio of the actual deposited material in the simulation to the theoretical amount that could have been deposited without flash, calculated as

$$\eta = \frac{1}{\rho\,\pi r^2\,v_z\,t} \sum_{i=0}^{N} m_i. \tag{2}$$

where $\rho$ is the material density of the rod, $r$ is the rod radius, $v_z$ is the rod feed rate, $t$ is the deposition time, $m_i$ is the mass of particle $i$ and N is the total number of deposited particles. Moreover, the effective deposition width is determined as the difference between the 90th and 10th percentile positions of the deposited particles along the y-direction. This gives a robust measure of the effective deposition width as it ignores extreme outliers or isolated particles far from the main deposit.

**Effect of changing thermal boundary conditions.** Fig. 2 compares the deposition efficiency, the deposition width, and the temperature fields of the rod and the deposit under three thermal boundary conditions: Set 0 (reference), Set 1 (heated substrate), and Set 2 (cooled substrate). Heating the substrate in Set 1 raises the temperature of both the rod and the deposited material. The hotter deposit softens, becomes more deformable, and offers less shear resistance. As the rod interacts with this softened layer, the reduced resistance lowers the deposition efficiency. The material also spreads more, which explains the wider deposition compared with Set 0. Cooling the substrate in Set 2 has the opposite effect. Lower temperatures stiffen the deposited material and reduce its deformability. This increases its shear resistance during contact with the deformable rod. As a result, deposition efficiency increases but the deposition width decreases, consistent with less deformable material. The trends match very well experimental findings from Krohn et al. [14] and Hoffmann et al. [15].

**Effect of changing rod diameter.** Fig. 3a shows how the rod diameter affects deposition efficiency, deposition width, and the temperature fields of both the rod and the deposit. Reducing the rod diameter increases deposition efficiency. This trend is linked to the lower temperatures observed with a smaller rod and to the higher contact pressure that develops when both the rod diameter and deposition width decrease. The simulations also show that the larger rod (Set 3) produces lower contact

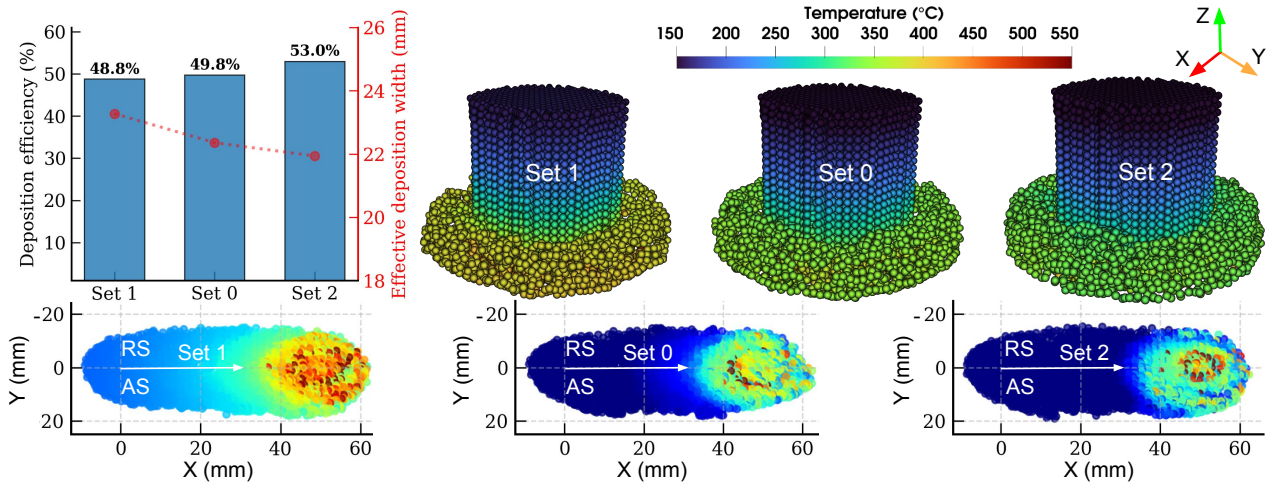


Fig. 2: Deposition efficiency, effective disposition width, and the temperature distribution of the deformed rod and 2D deposition projection for Set 0 (reference), Set 1 (heated), and Set 2 (cooled).

pressure and less variance, i.e., a more stable process overall, Fig. 3b. Its contact-pressure fluctuations are smaller than those of the smaller rod, even though the smaller rod achieves higher efficiency. The observed trend of changing the deposition efficiency with changing the rod diameter is consistent with the experimental findings by Angiwal et al. [16]. They observed that the contact radius decreases with increasing tangential velocity—in this study, associated with larger rod diameters—while Hoffmann et al. [15] reported that the contact radius is directly proportional to the deposition efficiency.

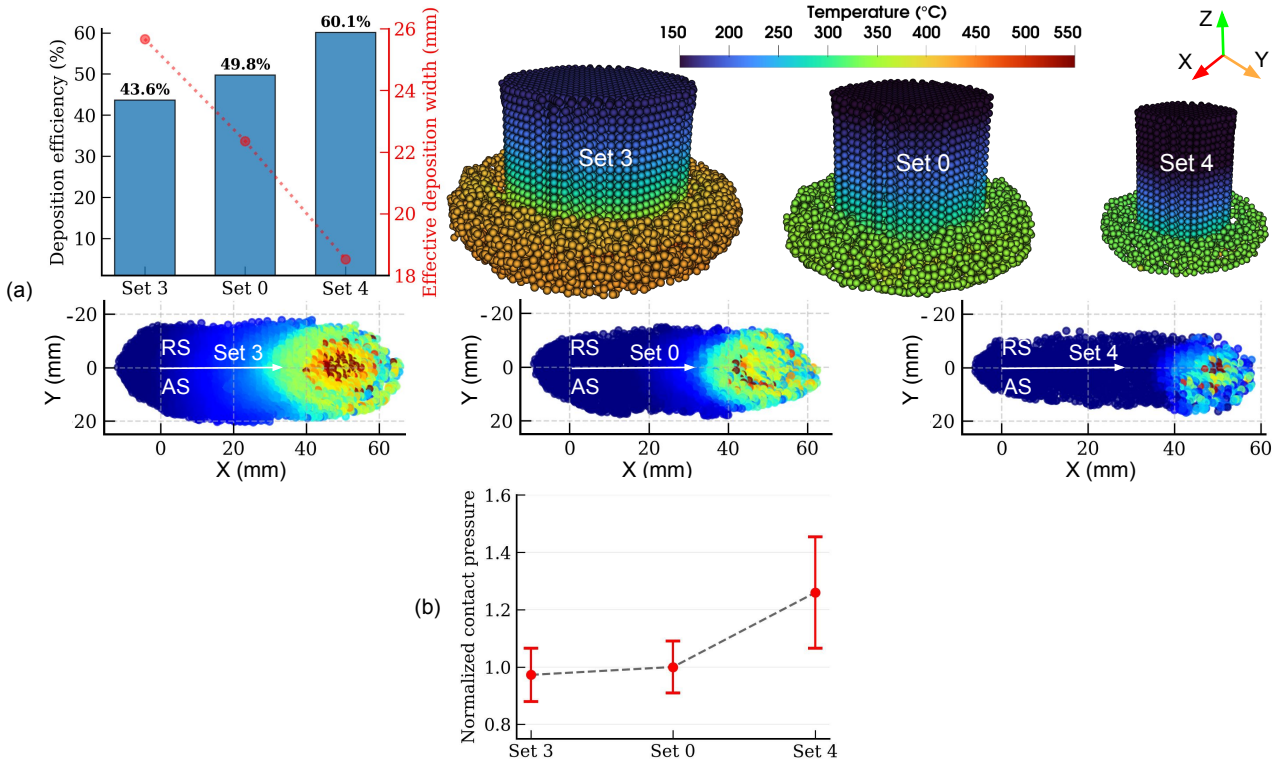


Fig. 3: (a) Deposition efficiency, effective disposition width, and the temperature distribution of the deformed rod and 2D deposition projection for Set 0 (reference), Set 3 (bigger diameter), and Set 4 (smaller diameter), and (b) The average and variance of the normalized rod contact pressure during the simulation of the same three sets with respect to Set 0.

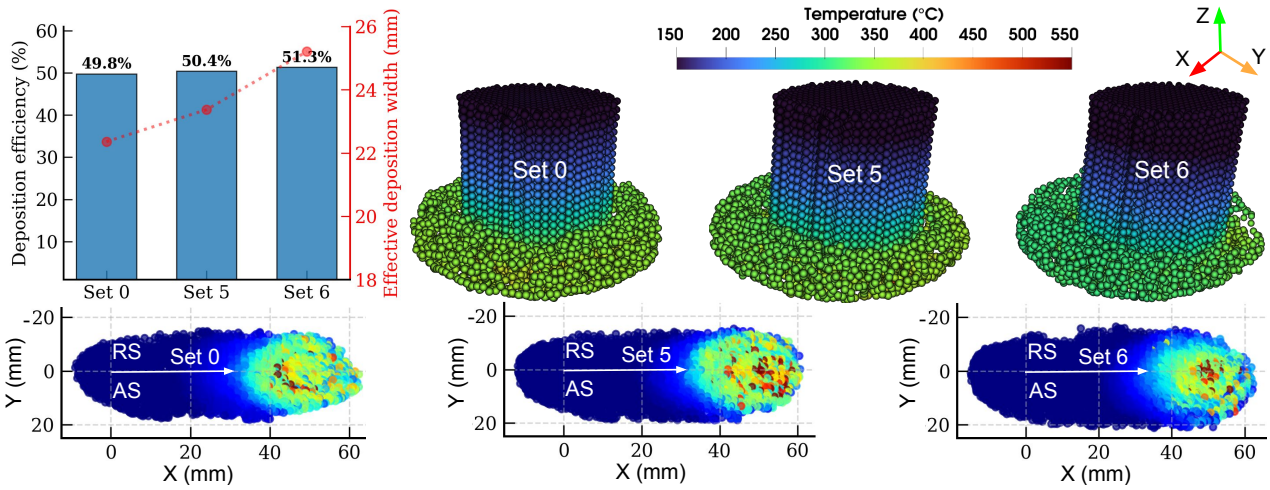


Fig. 4: Deposition efficiency, effective disposition width, and the temperature distribution of the deformed rod and 2D deposition projection for Set 0 (reference), Set 5 (bending 5°), and Set 6 (bending 10°).

**Effect of rod bending angle.** Fig. 4 shows the effect of changing the rod bending angle on the deposition efficiency, the deposition width, and the temperature fields of both the rod and the deposit. As the bending angle increases (Set 5 and Set 6), both the deposition width and the total deposited material rise, while the rod temperature drops. The larger bending angle increases the lateral spreading of the material, which widens the deposition. It also changes how the flash interacts with the existing deposit. With more bending, a larger portion of the flash gets into contact with the deposited layer and is deposited. This adds more material to the deposition and reduces the amount of hot flash forming, which lowers the rod temperature.

## Conclusion

This work numerically explored the influence of thermal boundary conditions, rod diameter, and rod bending angle on deposition efficiency and material flow behavior in friction surfacing using a GPU-accelerated SPH model. The results demonstrate that substrate temperature critically governs the deformability of the deposited layer, thereby controlling both deposition efficiency and spreading. Preheating the substrate promotes wider but less efficient deposition, whereas enhanced cooling yields higher efficiency with narrower deposits. Geometric variations further modulate the process: smaller rod diameters enhance efficiency through higher contact pressures, while larger rods provide more stable deposition dynamics. Additionally, rod bending increases material redistribution and promotes greater utilization of the rod material by directing more flash into the deposited layer. Overall, the study identifies thermal management and geometric configuration as practical levers for tuning friction surfacing performance. These insights provide a computational foundation for optimizing process setups, guiding experimental design, and informing future work on closed-loop control strategies and more comprehensive multiphysics simulation approaches.

## Funding

This project has received funding from the European Research Council (ERC) under the European Union's Horizon 2020 research and innovation program (grant agreement No 101001567).

**Data Availability**

The solver is released as open-source code via GitHub (https://github.com/SPH-SSMP/FE-SPH-GPU-ESAFORM) and the experimental data and simulation results are available at Zenodo (https://doi.org/10.5281/zenodo.18670132).

**References**

[1] J. Gandra, H. Krohn, R.M. Miranda, P. Vilaça, L. Quintino, J.F. dos Santos, *Friction surfacing—A review*, J. Mater. Process. Technol., Vol. 214, No. 5, pp. 1062–1093 (2014).

[2] R. Damodaram, P. Rai, S. Cyril Joseph Daniel, R. Bauri, D. Yadav, *Friction surfacing: A tool for surface crack repair*, Surf. Coat. Technol., Vol. 422, p. 127482 (2021).

[3] A. Sharifi, F. Khodabakhshi, S.F. Kashani-bozorg, A.P. Gerlich, *Microstructure and mechanical properties in additive manufacturing by friction surfacing of AA6061 alloy*, Mater. Sci. Eng. A, Vol. 884, p. 145520 (2023).

[4] Z. Kallien, L. Rath, A. Roos, B. Klusemann, *Application of friction surfacing for solid state additive manufacturing of cylindrical shell structures*, Addit. Manuf. Lett., Vol. 8, p. 100184 (2024).

[5] V.I. Vitanov, N. Javaid, *Investigation of the thermal field in micro friction surfacing*, Surf. Coat. Technol., Vol. 204, No. 16–17, pp. 2624–2631 (2010).

[6] S.M. Bararpour, H. Jamshidi Aval, R. Jamaati, *Modeling and experimental investigation on friction surfacing of aluminum alloys*, J. Alloys Compd., Vol. 805, pp. 57–68 (2019).

[7] P. Pirhayati, H. Jamshidi Aval, *An investigation on thermo-mechanical and microstructural issues in friction surfacing of Al–Cu aluminum alloys*, Mater. Res. Express, Vol. 6, No. 5 (2019).

[8] G.R. Liu, M.B. Liu, *Smoothed Particle Hydrodynamics: A Meshfree Particle Method*, World Scientific Publishing Co., Singapore (2003).

[9] H. Jamshidi Aval, *Comprehensive thermo-mechanical simulation of friction surfacing of aluminum alloys using smoothed particle hydrodynamics*, Surf. Coat. Technol., Vol. 419, p. 127274 (2021).

[10] S.M. Bararpour, H. Jamshidi Aval, R. Jamaati, M. Javidani, *Experimental and numerical investigation of Al16Si alloy friction surfacing on AA1050 substrate: Effect of axial feeding rate*, Surf. Coat. Technol., Vol. 468, p. 129778 (2023).

[11] S.M. Bararpour, H. Jamshidi Aval, R. Jamaati, M. Javidani, *Investigation of the effect of traverse speed in friction surfacing of Al–16Si alloy by smoothed-particle hydrodynamics simulation and experimental study*, Comput. Part. Mech., Vol. 11 (2023).

[12] A. Elbossily, Z. Kallien, R. Chafle, K.A. Fraser, M. Afrasiabi, M. Bambach, B. Klusemann, *GPU-accelerated meshfree computational framework for modeling the friction surfacing process*, Comput. Part. Mech. (2025), doi:10.1007/s40571-025-01048-2.

[13] G.R. Johnson, W.H. Cook, *A constitutive model and data for metals subjected to large strains, high strain rates and high temperatures*, Proc. 7th Int. Symp. Ballistics, pp. 541–547 (1983).

[14] H. Krohn, S. Hanke, M. Beyer, J.F. dos Santos, *Influence of external cooling configuration on friction surfacing of AA6082-T6 over AA2024-T351*, Manuf. Lett., Vol. 5, pp. 17–20 (2015).

[15] M. Hoffmann, E.A. Duda, P. Aspes, B. Klusemann, *Effect of ambient conditions in friction surfacing*, Weld. World, Vol. 69, No. 2, pp. 397–406 (2025).

[16] H. Agiwal, H. Yeom, K. Sridharan, S. Rudraraju, F.E. Pfefferkorn, *Radius of Contact During Friction Surfacing of Stainless Steel 304L: Effect of Spindle Speed and Rod Diameter*, J. Manuf. Sci. Eng., Vol. 146, No. 2, p. 021005 (2023).

[17] Y. Zou, W. Li, X. Yang, V. Patel, Z. Shen, Q. Chu, F. Wang, H. Tang, F. Cui, M. Chi, *Characterizations of dissimilar refill friction stir spot welding 2219 aluminum alloy joints of unequal thickness*, J. Manuf. Process., Vol. 79, pp. 91–101 (2022).

The publication of this article was funded by the National Research Council Canada NRC CNRC 10.13039/501100000046